Resolving Molecular Size and Homologues with a Self-Assembled Metal–Organic Framework Photonic Crystal Detector

Resolving molecular size and homologues with a self-assembled metal-organic framework photonic crystal detector

Xueying Fan[a]‡, Miao Xu[a]‡, Weizhe Liu[b], Aleksandr Kuchmizhak[c,d*], Lorenzo Pattelli[e,f*], Yao Li[g*], Hongbo Xu[a*]

ABSTRACT: Traditional environmental photonic sensing based on the balanced reflection of a photonic structure can hardly be applied to distinguish molecular size and homologues, since the refractive index change introduces by these analytes can be too similar to be unambiguously distinguished. Here, a sensing method based on the pore size selectivity and organics adsorption-desorption capacity of self-assembled ZIF-8 photonics crystal is demonstrated, which can tell apart different molecular sizes, homologues, and organics with similar structures and physical properties. Specificity is improved by the inherent relationships between the pore size of ZIF-8 metal-organic frameworks (MOFs) and the associated molecular diffusion rates in the pores, so that the combination of the observed peak shift and recovery time are unique to each analyte. Using this method, selective detection of molecular size is also demonstrated in the case of a linear (n-hexane) vs. circular molecule (cycle hexane), since only the former can penetrate inside the ZIF-8 pores to induce a large wavelength shift. The reflection peak shift of the linear molecule is about 30-40 nm, compared to just than 4 nm for the circular molecule. A relationship between the diffusion rate of linear molecules in ZIF-8 pore and the recovery time of photonic crystal reflective peak is further established, linking the recovery time and the linear molecular diffusion coefficient. Finally, different linear molecules are identified by their associated recovery time to detect homologues or organics with similar refractive index.

INTRODUCTION

Responsive photonic crystals (RPCs) are gaining great research interest due to their variable photonic band gap (PBG) and the many potential applications that they enable in photonic and chemical sensing [1,2] display technology [3], anti-counterfeiting [4], and solar cells [5]. Among these applications, RPC-based environmental sensors have been widely studied due to their low cost (as compared to gas/liquid chromatography or mass spectrometry [6–8]), fast response time and naked-eye visual detection feedback.

Photonic sensing is commonly realized by detecting a shift or a change in the PBG induced by a change in the liquid and gaseous chemical composition of its environment [9]. According to Bragg's law, the PBG of the RPC can be adjusted by changing the effective refractive index and the spacing between consecutive diffracting planes [10–12]. Both can change when the voids of RPC are infiltrated by some analytes, which will cause a shift in the reflection peak associated with the PBG [13]. In the past few years, functional materials have been introduced into photonic crystals, where a change in refractive index or lattice spacing translates into a change in its structural color [14–17]. For example, inverse opal structures made of functional materials have been used to detect different solvent vapors [18], pH [19], metal ions, macromolecule[20] and viruses[21], while direct opals comprising mesoporous silica can detect ethanol, methanol, acetone, toluene, water and chloroform vapors [10]. However, mentioned photonic-based sensors can hardly be applied to distinguish different chemical species with similar refractive indices, as they would induce the same PBG modification. To overcome this issue, additional effects should be combined with the PBG tuning. For instance, Kou et al. showed that it is possible to distinguish of benzene, toluene, xylene, and ethylbenzene based on differences in the swelling behavior of an RPC[22]. Additionally, the dynamic reflection spectrummethod was developed by Zhang et al. [23], based on different diffusion behavior of solvent molecules in inverse opal photonic crystals. Nevertheless, mentioned methods are still relatively complicated and do not allow to establish a direct relationship between the PBG shifts and molecular size. Thus, it remains challenging to implement a sensing technique providing different responses sensitive to molecular size and allowing to distinguish chemical species with similar refractive indices.

Due to their high surface area [24], tunable pore characteristics [25] and controlled chemical environment, metal-organic frameworks (MOFs) represent a promising candidate for selective sensing since the relationship between PBG shifts and molecular size (or chemical properties) can be tuned through the appropriate MOF design [26,27]. For this reason, in the past years, several MOF-based photonic sensors have been proposed to detect solvent vapor through the modulation of their reflectance response[28–35]. For example, a 1D photonic sensor consisting of alternating layers of MOFs and TiO_2 nanoparticles showed specific color changes in response to different vapors[36]. Lu et al. demonstrated highly efficient and rapid detection of ethanol and methanol using a photonic crystal made of ZIF-8@SiO_2 [37]. Quantitative analysis of methanol and ethanol was also later achieved by Ranft et al. [38] by increasing the MOF content in 1D photonic crystals made of MIL-88 and HKUST-1. All these approaches rely on polycrystalline MOF nanoparticles and improve the detection sensitivity by exploiting the large specific surface and spacing between MOFs nanoparticles. Nonetheless, these methods fail to fully take advantage of the inherent MOF porosity, since the analytes are mainly adsorbed on the surface of the MOFs nanoparticles and in the gaps between them. Moreover, the potential selectivity and molecular sieving capability if often reduced by the low degree of crystallinity of MOFs reported so far. If the MOFs are prepared from the monodisperse nanocrystals and self-assembled into a 3D photonic crystal, then the resulting 3D MOF photonic crystal can

fully benefit from the well-defined size and the chemical environment of the MOF pores.

Based on the above considerations, this study reports a photonic sensing platform prepared by self-assembly of monodisperse ZIF-8 nanocrystal capable of distinguishing molecular sizes and chemical species with similar refractive indices. Our proposed ZIF-8 photonic sensing platform exhibits a prominent reflection peak as determined by the diameter of the nanocrystals, while their pores provide the site of molecular adsorption/desorption and selective size detection. As an example, we show a reflection peak shift of about 50 nm for a linear molecule (n-hexane), compared to the much smaller response (<4 nm) to cyclic molecules such as cyclohexane, benzene, methylbenzene and xylene. More importantly, adsorption/desorption of linear molecules into the ZIF-8 pores leads to changes in the diffraction properties of photonic crystals and therefore its optical appearance, which evolves in time based on the diffusion rate of linear molecules in ZIF-8 pore. In the case of methanol, ethanol, propanol butanol, and n-hexane the reflection peak of ZIF-8 photonic sensing exhibited similar wavelength shifts, but different recovery times of 2 min, 5 min, 16 min, 150 min and 85 min, respectively. The distinction between methanol, ethanol, propanol, butanol and n-hexane can be therefore achieved based on their characteristic recovery time.

RESULT AND DISCUSSION

Figure 1 schematically explains the preparation procedure of the MOF-based photonic sensor and its response mechanism to different organic vapors. The sensor represents nanostructured film composed of self-assembled monodispersed ZIF-8 nanoparticles that form a 3D photonic crystal with a resonant optical reflectance originated from light diffraction on the ordered structure. ZIF-8 crystals possess a large specific surface and a porous structure, that provide channels for sieving of linear molecules with their size smaller comparing to the ZIF-8 average pore diameter (about 0.5 nm). Adsorbed linear molecules strongly modify the refractive index of ZIF-8 photonic crystal resulting in considerable shift of the reflectance peak. Larger cyclic molecules can't penetrate through the ZIF-8 nanopores predominantly adsorbing on the outer surface of photonic crystal, thereafter causing weak spectral shift of the reflectance peak. In addition, the speed at which the sensor restores its initial optical properties, a recovery time, depends on the homolog-specific diffusion rate of the linear molecules inside the photonic crystal. Therefore, both recovery time and reflectance peak shift can be used to distinguish homologues and molecule size as it is schematically explained in Figure 1.

The average size of ZIF-8 nanocrystals produced by an improved solvothermal method can be controlled by the concentration of the CTAB. In this work, we produced high-quality polyhedral nanocrystals with four characteristic sizes (270 nm, 210 nm, 190 nm and 140 nm) and narrow size distribution <5% of each fraction (see Figure S1 a-d). The XRD peaks of all mentioned synthesized nanocrystal fractions are consistent with those for the standard ZIF-8 material confirming their good crystallinity (Figure S2). Furthermore, the FTIR spectra of the nanocrystals indicate characteristic C-H (at 3138 and 2933 cm^{-1}) and C=N (1580 cm^{-1}) bonds, that further proves correct chemical composition consistent with ZIF-8 material (Figure S3).

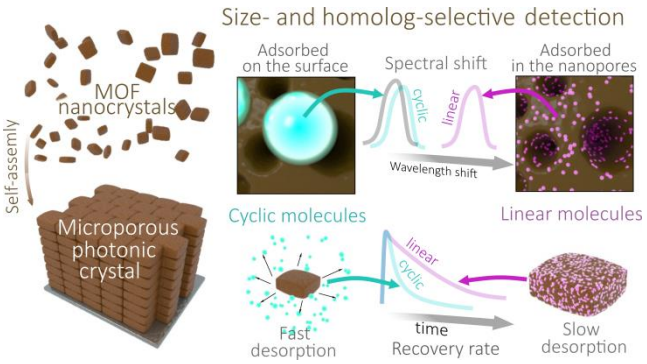

Figure 1. Schematic diagram illustrating preparation procedure of MOF photonic sensor and its sizes and homologue selective optical response to different organic vapors.

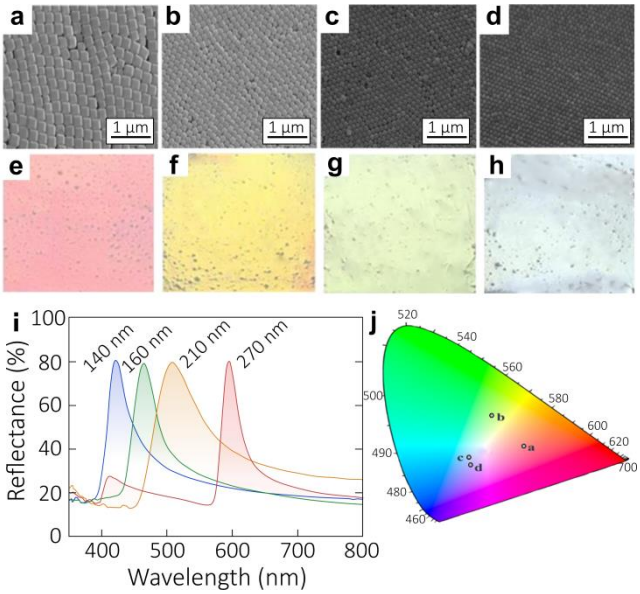

Figure 2. SEM (top row) and optical images (bottom row) of the RPCs self-assembled from different ZIF-8 nanocrystals with their size of 270 (a,e), 190 (b,f), 160 (c,g) and 140 nm (d,h), respectively. (e) Optical reflectance spectra of corresponding RPCs. (j) CIE 1931 chromaticity map with the coordinates that correspond to reflectance spectra of the RPCs.

The ZIF-8 RPC is self-assembled by controlling the contact angle between ZIF-8 dispersion and a substrate. Figure 2 a-d shows close-up SEM images of the resulting RPCs revealing good arrangement of the nanocrystals in a hexagonal close-packed plane (111). These images also reveal small number of defects related to lattice disordering; however, such defects do not deteriorate resonant reflectivity of the photonic crystal. RPCs consisting of the nanocrystals with the size of 270 nm, 210 nm, 160 nm and 140 nm appear red, yellow, blue and violet, respectively, on the optical images (Figure 2 e-h). This visual structural color appearance was confirmed by measuring the reflectance spectra from the corresponding RPCs (Figure 2i), clearly revealing the maximum gradually shifting from 410 to 600 nm, upon increasing the size of the nanocrystals composing corresponding photonic crystal. Representation of the reflectance spectra of the mentioned RPCs colors as coordinates in Commission Internationale de L'Eclairage (CIE) color space is provided in Figure 2f, returning results that are basically consistent with the optical images. Overall, by tuning the characteristic size of

ZIF-8 building blocks one can tailor both the morphological and optical properties of the resulting RPC.

The naked eye is more sensitive to green, while the reflection peak of the related RPC made of the nanocrystals with a size of 160 nm is spectrally narrow. In addition, photonic crystals assembled from the smaller nanocrystals usually exhibits smaller number of lattice defects that is important for qualitative and reliable measurements. Optical response of the chosen RPC to its exposure by different saturated organic vapors is summarized in Figure 3. On the one hand, the RPC responds with a marked reflectance peak shift with its value ranging from 30 to 50 nm, when exposed to linear molecule vapors as methanol, ethanol, n-propanol, n-butanol and n-hexane (Figure 3a). In particular, the peak shifts caused by methanol, ethanol, n-propanol, n-hexane and n-butanol vapors are 31, 34, 40, 44 and 48 nm, respectively. On the other hand, exposure by cyclic molecule vapors as cyclohexane, xylene, toluene, and benzene induces a small shift which does not exceed 3.5±0.5 nm (Figure 3b). Huge difference between the optical responses of the mentioned photonic crystal to cyclic and linear molecule vapors and sensor capability to distinguish molecular size are highlighted in a more clear way in Figure S4, showing an order of magnitude larger reflectance peak shifts caused by small linear molecules. Such molecules can not only be adsorbed on the RPC surface but also penetrate though the nanopores of ZIF-8 nanocrystals that leads to stronger modulation of the optical properties of the photonic crystal. According to our measurements of nitrogen sorption/desorption isotherms using Brunauer-Emmett-Teller method (see Figures S4 and S5), the ZIF-8 nanocrystals demonstrate specific surface area of 1220.77 $m^2 g^{-1}$ and the average pore diameter of 0.45 nm that is larger comparing to the typical size of the linear molecules (e.g., n-hexane molecule has the size of 0.2 nm). Conversely, the size of cyclic molecule is larger than the nanopores size (e.g., cyclohexane molecule size is 0.7 nm; Figure S6), and related vapors can not penetrate inside the photonic crystal. Consequently, large cyclic molecules can only be adsorbed on the external surface of the RPC causing a much smaller shift of the reflection peak (Figure 3b).

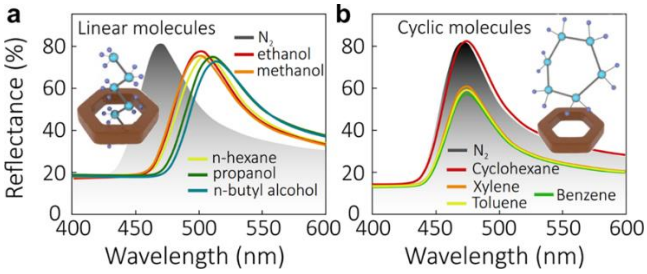

Figure 3. Series of reflection spectra of the RPC made of the ZIF-8 nanocrystals with a size of 160 nm exposed to saturated vapors of (a) linear (methanol, ethanol, propanol, butanol and n-hexane) and (b) cyclic molecules (cyclohexane, xylene, toluene, and benzene).

Figure 4a demonstrates modification of the reflectance spectra of the chosen RPC upon gradual increasing of the methanol vapor concentration in nitrogen from 0 to 100%. As can be seen, the reflectance peak gradually redshifts from 469 nm to 500 nm demonstrating basically linear relationship (R^2=0.99) between the peak shift and methanol concentration (Figure 4b). We observed similar linear trend and modulation of the reflectance spectra of the RPC upon its exposure to other linear molecule vapors at variable concentrations (ethanol, propanol, butanol and n-hexane) (Figure S8).

Response and recovery time are also important factors in assessing the ZIF-8 RPC. The recovery time is the time needed to restore the original reflectance peak position, defined under nitrogen gas exposure. Figure 4c shows the dynamics of the reflectance peak position as a function of time revealing the response and recovery time of the photonic crystal sensor upon its consecutive exposure to saturated vapor of methanol and nitrogen. The data indicates the sensor response time to methanol vapor less than 30 s, while it takes about 3 min for complete recovery upon exposure to nitrogen. Sensor demonstrates good reproducibility of the optical response (peak shift and response/recovery time) to methanol (Figure 4d) as well as to other tested linear molecule vapors (Figure S8) under 20 consecutive measurement cycles. Furthermore, according to the TGA analysis the ZIF-8 nanocrystals withstand temperatures up to 400 °C (Figure S10), demonstrating potential of using sensor heating to speed up the recovery time and sensing performance.

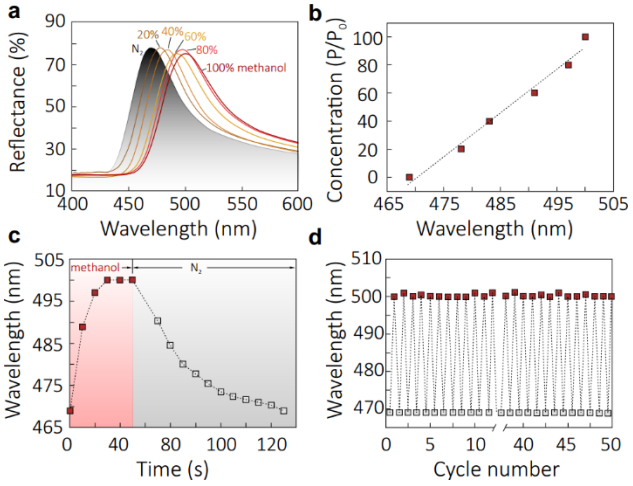

Figure 4. (a) Series of reflection spectra of the RPC made of the ZIF-8 nanocrystals with a size of 160 nm exposed to varying relative concentrations of methanol vapor mixed with nitrogen. (b) Relative concentration of methanol vapor as a function of spectral position of reflectance peak. (c) Dynamics of the reflectance peak position upon sensor exposure to saturated methanol vapor (t = 0) and to nitrogen (t = 50 s) as a function of time t. (d) Cycling sensing performance of the ZIF-8 RPC upon its consecutive exposure to saturated methanol and nitrogen.

Figure 5 depicts the relaxation dynamics of the optical response of the chosen ZIF-8 RPC after the end of its exposure (marked as t=0) to six different vapors (methanol, ethanol, propanol, butanol, n-hexane, and cyclohexane). As can be seen, once the vapor exposure is switched off, the spectral position of reflection peak (dashed curve) starts to gradually blue shift towards its initial position, while the reflection peak intensity remains almost unchanged. In the case of all tested linear molecules (Figure 5a-e), the blueshift of the reflectance wavelength is noticeably larger comparing to similar response of the sensor exposed to cyclohexane (Figure 5f). Substantial difference in observed recovery times reflects completely different diffusion rate of the linear and cyclic molecules inside the nanopores of the RPC and near its outer surface as it is schematically illustrated in Figure 5g. As it was mentioned above, cyclic molecules are adsorbed on the surface of the photonic crystal, resulting in their fast desorption and recovery time. To the contrary, linear molecules penetrate deeper inside RPC through the pores, thus their diffusion outside takes more time.

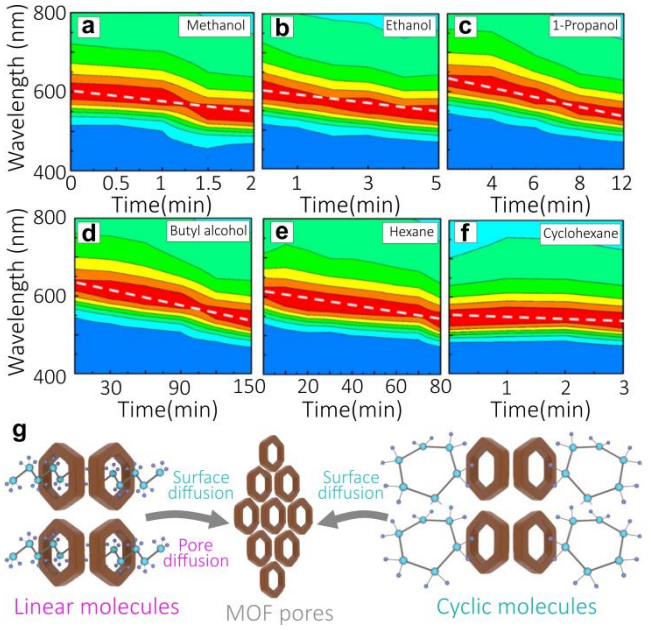

Figure 5. Recovery of the ZIF-8 RPC sensor response after the end of its exposure with different linear and cyclic molecule vapors: (a) n-hexane; (b) methanol; (c) ethanol; (d) propanol; (e) butanol; (f) cyclohexane. (g) Diffusion diagram of linear and cyclic molecules in the ZIF-8 RPC.

The data on wavelength shift versus time (or sensor recovery time) is further summarized in Figure 6a for several organic vapors. Noteworthy, considered vapors have similar refractive indices causing identical spectral shifts of the reflectance peal of the RPC (Table S2). For instance, the refractive indices of methanol and ethanol are 1.349 and 1.362, respectively, which makes it difficult to tell them apart. On the other hand, the recovery time of the sensor exposed to methanol, ethanol, propanol, n-hexane and n-butyl alcohol, are 2, 5, 16, 85 and 150 min, respectively, being compared much shorter recovery time (<30 s) of the sensor exposed to cyclohexane, benzene, toluene and xylene (Figure S11). These large differences are due to the fact that recovery times are governed by the diffusion speed of the molecules in ZIF-8 RPC, so that homologues and species with similar refractive index can still be distinguished based on their diffusion coefficient inside the pores.

As an example of how the MOF-based sensor takes advantage of the relation between solvent properties and diffusion constant in ZIF-8, the relationship between the recovery time of methanol and the corresponding wavelength of the reflection peak can be explicitly cast using a simple model. According to Bragg's Law, the reflection wavelength of the ZIF-8 sensor at recovery time t can be calculated using the following equation:

$$\lambda_t = \frac{\lambda_0}{[(1-f_1-f_2)n_{ZIF-8}+f_2 n_A]}\{(1-f_1-f_2)n_{ZIF-8}+(f_1+f_2)[(n_A-1)\frac{C_{At}}{C_{A0}}+1]\} \quad (1)$$

where λ_0 is the reflection wavelength upon saturation of organic vapors (see Equation S1; Supporting Information), n_{ZIF-8} is the refractive index of ZIF-8, n_A is the refractive index of methanol, C_{A0} is the maximum adsorption capacity of methanol in ZIF-8 RCP, C_{At} is adsorption amount of methanol in ZIF-8 RCP after desorption time t, while f_1 and f_2 represent the volume rate of pores of ZIF-8 and ZIF-8 RPC, respectively. By differentiating this equation one can obtain

$$\frac{d\lambda_t}{dt} = \frac{\lambda_0(f_1+f_2)(n_A-1)}{[(1-f_1-f_2)n_{ZIF-8}+f_2 n_A]C_{A0}}\frac{dC_{At}}{dt} \quad (2)$$

According to Fick's second law, the relationship between methanol concentration in ZIF-8, the diffusion coefficient and the diffusion time can be calculated as

$$\frac{dC_{At}}{dt} = \frac{d}{dx}(D_A\frac{dC_{At}}{dx}) \quad (3)$$

where D_A is diffusion coefficient of methanol and x is the distance through the equivalent diffusion layer. By combining equations (2) and (3), we finally obtain the wavelength variation as a function of the diffusion process along the ZIF-8 RPC (Figure S12)

$$\frac{d\lambda_t}{dt} = \frac{\lambda_0(f_1+f_2)(n_A-1)D_A}{[(1-f_1-f_2)n_{ZIF-8}+f_2 n_A]C_{A0}}\frac{d}{dx}(\frac{dC_{At}}{dx}) \quad (4)$$

The obtained equation confirms that faster sensor response and shorter recovery time are expected for molecules with larger diffusion coefficients, that is consistent with the results shown in Figure 6a. Taking into account the measured recovery time of the RPC gas sensor exposed to methanol (2 min), ethanol (5 min), propyl alcohol (16 min), n-hexane (85 min) and n-butyl (150 min), we can compare the diffusion coefficients for these molecules estimated using the Fuller formula (see Supporting Information). These estimations give diffusion coefficients of methanol, ethanol, propanol, n-hexane and n-butyl of 1.5955×10^{-5}, 1.22233×10^{-5}, 1.02167×10^{-5}, 7.64045×10^{-6}, 8.93121×10^{-6}, respectively. The diffusion coefficients of these molecules show a decreasing trend, which is associated with the observed increase of their recovery time.

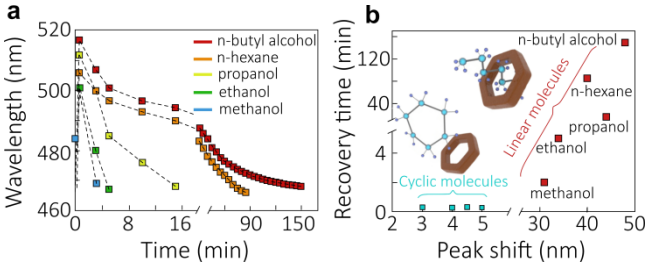

Figure 6. (a) Time evolution of the reflection peak wavelength for various vapors; (b) relationship between the spectral shift of reflectance peak and sensor recovery time for various organic vapors.

Thus, calculated and measured results are in good agreement, with the small deviation of n-butanol, which may be explained by its high boiling point with respect to the other species. Plotting the overall peak shift range and characteristic recovery times for all the tested molecules shows a net clustering between the two types of structures, as shown in Figure 6b. Linear molecules show a longer recovery time and a larger wavelength shift range, enabling the identification of molecular size and homologues. Similar assembly process developed for ZIF-8 MOFs was adopted to prepare the RPCs from another nanocrystals, UiO-66 MOF (Figure S13-S15), demonstrating flexibility of the developed protocol broadened the research idea and application prospect of MOFs photonic crystals.

CONCLUSION

In summary, a ZIF-8 RPC was designed by self-assembly of monodisperse ZIF-8 nanocrystals, which showed a strong optical response in terms of reflection peak shift and recovery time when exposed to different analytes. By combining the information from these two observables, the sensor is able to identify species with similar molecular sizes, homologues and organic compounds with nearly identical refractive index. Large differences in the observed recovery times are due to the fact that only small linear molecules can enter the ZIF-8 pore, while large cyclic can be adsorbed only on the external surface of the MOF channels. The observed wavelength shift is fully reversible after a few minutes following the alternating exposure to organic vapor and nitrogen. The inverse relationship between the recovery time of ZIF-8 RPC and the diffusion coefficient of organic molecules was also derived through a simple model. For analytes with similar refractive indices, such as propanol (n=1.385) and n-hexane (n=1.387), despite similar peak wavelength shift values, very different recovery times are observed of 16 min and 85 min, respectively. Thanks to different diffusion dynamics associated to different molecules, MOF-based photonic crystals hold promise for the unambiguous detection of small and linear homologs according to their recovery times.

METHOD

Materials. Zinc acetate (Zn $(CH_3COO)_2$), Hexadecyl trimethyl ammonium Bromide(CTAB), 1,4-Dicarboxybenzene (BDC) and Zirconium(IV) chloride($ZrCl_4$) were purchased from Aladdin. Acetic Acid (CH_3COOH) and anhydrous ethanol (C_2H_5OH) were purchased from Sinopharm Chemical Reagent Co., Ltd. The experiment water used was Mill-Q secondary ultrapure water (18.25 $M\Omega{\cdot}cm^3$). 2-Methylimidazole ($C_4H_6N_2$) was purchased from Alpha Pharmaceutical Limited. N,N-dimethylformamide (DMF), methanol(CH3OH), n-propanol(C_3H_8O), 1-butanol($C_4H_{10}O$), n-Hexane(C_6H_{14}), cyclohexane(C_6H_{12}), Benzene (C_6H_6), methylbenzene(C_7H_8), dimethylbenzene(C_8H_{10}) and iso-propyl alcohol(C_3H_8O) were provided by Xilong Scientific Co., Ltd. All reagents with analytical grade were purchased and used without further purification.

Synthesis of monodispersed ZIF-8 with an addition of CTAB. Zn $(CH_3COO)_2$ (0.6 g, 3.27 mmol) was first dissolved in 10 mL of deionized water at room temperature as a zinc source. Aqueous solutions with different concentrations of hexadecyl trimethyl ammonium bromide (CTAB) were 0.4, 0.5, 0.6 and 0.7 mmol/L, respectively. After completely dissolving the 2-methylimidazole (0.223 g, 0.272 mol) in 10 ml of CTAB solution, 10 ml of prepared $Zn(CH_3COO)_2$ solution was added. The solution was magnetically stirred for 5 minutes to ensure complete mixing, and then left to react at room temperature for 2 h. After the reaction, the as-synthesized materials were collected by centrifugation and thoroughly washed three times with deionized water (Table S1).

Preparation of ZIF-8 photonic crystals. Glass plates were first sonicated with acetone, anhydrous ethanol, and deionized water for 15 min, respectively. Then, glass substrates are dried at 60 °C for 2 h and treated with plasma for 5 min to enhance hydrophilicity. PDMS and curing agent with a mass ratio of 10:1 were placed in a vessel, mixed evenly with a glass rod and left to rest for about 1 h. When the bubbles disappear completely, a syringe is used to deposit PDMS on the glass plate. Blade coating is used to spread the PDMS evenly over the glass plate followed by its drying at 60℃ for 10 hours. PDMS is used to adjust the ZIF-8 solution onto the plate before assembly, so that the MOF dispersion can be more evenly coated on the surface of the plate, so as to obtain higher quality photonic crystals. A solution of 10% monodisperse ZIF-8 in ethanol and water (1:1) was drop-casted to the prepared substrate. Then, the PDMS-coated substrate was placed in a constant temperature water tank at 60 °C for 10 h. Finally, the 3D photonic crystals are obtained from PDMS-coated glass by self-assembly of monodispersed ZIF-8 nanocrystal.

Characterization. Scanning electron microscope (SEM) images was carried out with Helios Nanolab600i. X-ray diffraction (XRD) data was obtained on a Bruker D8 Advance diffractometer with Cu K_a radiation at a scan rate of 10° min^{-1}. The specific surface area and pore size of the samples were assessed by the Brunauer-Emmett-Teller (BET) method (APAS-2020). Thermogravimetric analysis (TGA) was used to study the thermal stability of the materials (Perkin Elmer STA600). Fourier Transform Infrared (FTIR) spectrometer (Nicolet iS5) was used to analyze the composition and structure of the samples. JCY-1 setup from Shanghai Fongrui Company was used for contact angle tests. The dispersion of ZIF-8 nanopaticles was characterized by dynamic light scattering method (Zetasizer Nano S90 Malvern). The optical properties of the samples were tested by a fiber-coupled spectrometer (Ocean Optics Maya 2000).

ASSOCIATED CONTENT

Supporting Information

AUTHOR INFORMATION

Corresponding Author

Hongbo Xu, School of Chemistry and Chemical Engineering, Harbin Institute of Technology, Harbin, 150001, PR China, iamxhb@hit.edu.cn

Present Addresses

a MIIT Key Laboratory of Critical Materials Technology for New Energy Conversion and Storage, School of Chemistry and Chemical Engineering, Harbin Institute of Technology, 150001, Harbin, China

b Center for Composite Material and Structure, Harbin Institute of Technology, 150001 Harbin, China

c Institute for Automation and Control Processes, Far Eastern Branch, Russian Academy of Sciences, Vladivostok 690041, Russian Federation

d Pacific Quantum Center, Far Eastern Federal University, 690041 Vladivostok, Russia

e Istituto Nazionale di Ricerca Metrologica (INRiM), Turin, 10135, Italy

f European Laboratory for Non-linear Spectroscopy (LENS), Sesto Fiorentino, 50019, Italy

g Jinlin Changchun Judicail Identification Center, 130012 Changchun, China

Author Contributions

‡ Xueying Fan and Miao Xu have contributed equally.

ACKNOWLEDGMENT

We thank National Natural Science Foundation of China (No. 51702068, 52072096), China and the Fundamental Research Funds

for the Central Universities (HIT. NSRIF. 2020019, HIT OCEF. 2021004, FRFCU5710090220), the Innovation and Development Foundation of China Academy of Engineering Physics (Grant No.CX20200020), Heilongjiang Postdoctoral Fund (LBH-Z15078, LBH-Z16080).

REFERENCES

(1) Liu, Z.; Xie, Z.; Zhao, X.; Gu, Z. Z. Stretched Photonic Suspension Array for Label-Free High-Throughput Assay. *J. Mater. Chem.* **2008**, *18*, 3309. https://doi.org/10.1039/b807732k.

(2) Kumar, A.; Suthar, B.; Kumar, V.; Bhargava, A.; Singh, Kh. S.; Ojha, S. P. Design of a Thermally Tunable Filter Using Si-Based One-Dimensional Photonic Crystal. *Optik* **2013**, *124*, 2504–2506. https://doi.org/10.1016/j.ijleo.2012.08.030.

(3) Li, H.; Wang, J.; Lin, H.; Xu, L.; Xu, W.; Wang, R.; Song, Y.; Zhu, D. Amplification of Fluorescent Contrast by Photonic Crystals in Optical Storage. *Adv. Mater.* **2010**, *22*, 1237–1241. https://doi.org/10.1002/adma.200903105.

(4) Yin, Z.; Zhu, Y.; Xu, W.; Wang, J.; Xu, S.; Dong, B.; Xu, L.; Zhang, S.; Song, H. Remarkable Enhancement of Upconversion Fluorescence and Confocal Imaging of PMMA Opal/$NaYF_4$:Yb^{3+}, Tm^{3+}/Er^{3+} Nanocrystals. *Chem. Commun.* **2013**, *49*, 3781. https://doi.org/10.1039/c3cc40829a.

(5) Endo, T.; Yanagida, Y.; Hatsuzawa, T. Colorimetric Detection of Volatile Organic Compounds Using a Colloidal Crystal-Based Chemical Sensor for Environmental Applications. *Sensors and Actuators B: Chemical* **2007**, *125*, 589–595. https://doi.org/10.1016/j.snb.2007.03.003.

(6) Pan, M.; Li, X. bai; Xiong, C.; Chen, X.; Wang, L.; Chen, X.; Pan, L.; Xu, H.; Zhao, J.; Li, Y. Robust and Flexible Colloidal Photonic Crystal Films with Bending Strain–Independent Structural Colors for Anticounterfeiting. *Part. Part. Syst. Charact.* **2020**, *37*, 1900495. https://doi.org/10.1002/ppsc.201900495.

(7) Fröch, J. E.; Kim, S.; Stewart, C.; Xu, X.; Du, Z.; Lockrey, M.; Toth, M.; Aharonovich, I. Photonic Nanobeam Cavities with Nanopockets for Efficient Integration of Fluorescent Nanoparticles. *Nano Lett.* **2020**, *20*, 2784–2790. https://doi.org/10.1021/acs.nanolett.0c00466.

(8) Schurig, D.; Mock, J. J.; Justice, B. J.; Cummer, S. A.; Pendry, J. B.; Starr, A. F.; Smith, D. R. Metamaterial Electromagnetic Cloak at Microwave Frequencies. *Science* **2006**, *314*, 977–980. https://doi.org/10.1126/science.1133628.

(9) Pan, M.; Li, X. bai; Xiong, C.; Chen, X.; Wang, L.; Chen, X.; Pan, L.; Xu, H.; Zhao, J.; Li, Y. Dual Optical Information-Encrypted/Decrypted Invisible Photonic Patterns based on Controlled Wettability. *Adv. Opt. Mater.* **2022**, *10*, 2101268. https://doi.org/10.1002/adom.202101268.

(10) Xiong, C.; Zhao, J.; Wang, L.; Geng, H.; Xu, H.; Li, Y. Trace Detection of Homologues and Isomers Based on Hollow Mesoporous Silica Sphere Photonic Crystals. *Mater. Horiz.* **2017**, *4*, 862–868. https://doi.org/10.1039/C7MH00447H.

(11) Hu, Y.; Zhang, Y.; Chen, T.; Yang, D.; Ma, D.; Huang, S. Highly Efficient Detection of Homologues and Isomers by the Dynamic Swelling Reflection Spectrum. *ACS Appl. Mater. Interfaces* **2020**, *12*, 45174–45183. https://doi.org/10.1021/acsami.0c12229.

(12) Hu, Y.; Zhang, Y.; Yang, D.; Ma, D.; Huang, S. Self-Assembly of Colloidal Particles into Amorphous Photonic Crystals. *Mater. Adv.* **2021**, *2*, 6499–6518. https://doi.org/10.1039/D1MA00477H.

(13) Qin, J.; Li, X.; Cao, L.; Du, S.; Wang, W.; Yao, S. Q. Competition-Based Universal Photonic Crystal Biosensors by Using Antibody–Antigen Interaction. *J. Am. Chem. Soc.* **2020**, *142*, 417–423. https://doi.org/10.1021/jacs.9b11116.

(14) Liu, C.; Fan, Z.; Tan, Y.; Fan, F.; Xu, H. Tunable Structural Color Patterns Based on the Visible-Light-Responsive Dynamic Diselenide Metathesis. *Adv. Mater.* **2020**, *32*, 1907569. https://doi.org/10.1002/adma.201907569.

(15) Nikhil A.; Ehsan E.; Say H. T.; Li, X.; James S. J.; Nam T. N.; Zhao, H.; Zhao, D.; Li, Q. Ensembles of Photonic Beads: Optical Properties and Enhanced Light. *Adv. Optical Mater.* **2020**, *8*, 1901537. https://doi.org/10.1002/adom.201901537.

(16) Hou, J.; Li, M.; Song, Y. Recent Advances in Colloidal Photonic Crystal Sensors: Materials, Structures and Analysis Methods. *Nano Today* **2018**, *22*, 132–144. https://doi.org/10.1016/j.nantod.2018.08.008.

(17) Ge, J.; Yin, Y. Responsive Photonic Crystals. *Angew. Chem. Int. Ed.* **2011**, *50*, 1492–1522. https://doi.org/10.1002/anie.200907091.

(18) Liu, C.; Tong, Y. L.; Yu, X. Q.; Shen, H.; Zhu, Z.; Li, Q.; Chen, S. MOF-Based Photonic Crystal Film toward Separation of Organic Dyes. *ACS Appl. Mater. Interfaces* **2020**, *12*, 2816–2825. https://doi.org/10.1021/acsami.9b18012.

(19) Nakayama, D.; Takeoka, Y.; Watanabe, M.; Kataoka, K. Simple and Precise Preparation of a Porous Gel for a Colorimetric Glucose Sensor by a Templating Technique. *Angew. Chem. Int. Ed.* **2003**, *42*, 4197–4200. https://doi.org/10.1002/anie.200351746.

(20) Couturier, J. P.; Sütterlin, M.; Laschewsky, A.; Hettrich, C.; Wischerhoff, E. Responsive Inverse Opal Hydrogels for the Sensing of Macromolecules. *Angew. Chem. Int. Ed.* **2015**, *54*, 6641–6644. https://doi.org/10.1002/anie.201500674.

(21) Zhang, R.; Zhang, D.; Yao, Y.; Zhang, Q.; Xu, Y.; Wu, Y.; Yu, H.; Lu, G. Metal–Organic Framework Crystal-Assembled Optical Sensors for Chemical Vapors: Effects of Crystal Sizes and Missing-Linker Defects on Sensing Performances. *ACS Appl. Mater. Interfaces* **2019**, *11*, 21010–21017. https://doi.org/10.1021/acsami.9b05933.

(22) Kou, D.; Zhang, Y.; Zhang, S.; Wu, S.; Ma, W. High-Sensitive and Stable Photonic Crystal Sensors for Visual Detection and Discrimination of Volatile Aromatic Hydrocarbon Vapors. *Chem. Eng. J.* **2019**, *375*, 121987. https://doi.org/10.1016/j.cej.2019.121987.

(23) Zhang, Y.; Fu, Q.; Ge, J. Photonic Sensing of Organic Solvents through Geometric Study of Dynamic Reflection Spectrum. *Nat Commun* **2015**, *6*, 7510. https://doi.org/10.1038/ncomms8510.

(24) Kitagawa, S.; Kitaura, R.; Noro, S. Functional Porous Coordination Polymers. *Angew. Chem. Int. Ed.* **2004**, *43*, 2334–2375. https://doi.org/10.1002/anie.200300610.

(25) Férey, G. Hybrid Porous Solids: Past, Present, Future. *Chem. Soc. Rev.* **2008**, *37*, 191–214. https://doi.org/10.1039/B618320B.

(26) Avci, C.; Imaz, I.; Carné-Sánchez, A.; Pariente, J. A.; Tasios, N.; Pérez-Carvajal, J.; Alonso, M. I.; Blanco, A.; Dijkstra, M.; López, C.; Maspoch, D. Self-Assembly of Polyhedral Metal–Organic Framework Particles into Three-Dimensional Ordered Superstructures. *Nature Chem.* **2018**, *10*, 78–84. https://doi.org/10.1038/nchem.2875.

(27) Avci, C.; Liu, Y.; Pariente, J. A.; Blanco, A.; Lopez, C.; Imaz, I.; Maspoch, D. Template-Free, Surfactant-Mediated Orientation of Self-Assembled Supercrystals of Metal–Organic Framework Particles. *Small* **2019**, *15*, 1902520. https://doi.org/10.1002/smll.201902520.

(28) Avci, C.; De Marco, M. L.; Byun, C.; Perrin, J.; Scheel, M.; Boissière, C.; Faustini, M. Metal–Organic Framework Photonic Balls: Single Object Analysis for Local Thermal Probing. *Advanced Materials* **2021**, *33*, 2104450. https://doi.org/10.1002/adma.202104450.

(29) Ren, J.; Meijerink, A.; Zhou, X.; Wu, J.; Zhang, G.; Wang, Y. In Situ Embedding Synthesis of $CsPbBr_3$ @Ce-MOF@SiO_2 Nanocomposites for High Efficiency Light-Emitting Diodes: Suppressing Reabsorption Losses through the Waveguiding Effect. *ACS Appl. Mater. Interfaces* **2022**, *14*, 3176–3188. https://doi.org/10.1021/acsami.1c20804.

(30) Chen, S.; Bu, D.; Hu, Y.; Xiao, X.; Yang, D.; Ma, D.; Huang, S. Photonic Crystals with Tunable Lattice Structures Based on Anisotropic Metal–Organic Framework Particles and Their Application in Anticounterfeiting. *Advanced Photonics Research* **2022**, *3*, 2100246. https://doi.org/10.1002/adpr.202100246.

(31) Li, H.Y.; Zhao, S.N.; Zang, S.Q.; Li, J. Functional Metal–Organic Frameworks as Effective Sensors of Gases and Volatile Compounds. *Chem. Soc. Rev.* **2020**, *49*, 6364–6401. https://doi.org/10.1039/C9CS00778D.

(32) Olorunyomi, J. F.; Sadiq, M. M.; Batten, M.; Konstas, K.; Chen, D.; Doherty, C. M.; Caruso, R. A. Advancing Metal-Organic Frameworks toward Smart Sensing: Enhanced Fluorescence by a Photonic Metal-Organic Framework for Organic Vapor Sensing. *Adv. Optical Mater.* **2020**, *8*, 2000961. https://doi.org/10.1002/adom.202000961.

(33) Bai, L.; He, Y.; Zhou, J.; Lim, Y.; Mai, V. C.; Chen, Y.; Hou, S.; Zhao, Y.; Zhang, J.; Duan, H. Responsive Amorphous Photonic Structures of Spherical/Polyhedral Colloidal Metal–Organic Frameworks. *Adv. Optical Mater.* **2019**, *7*, 1900522. https://doi.org/10.1002/adom.201900522.

(34) Yu, S.; Wang, X.; Jiao, X.; Li, C.; Chen, D. Polyhedral Metal–Organic Framework Monolayer Colloidal Crystals with Sharpened and Crystal Facet-Dependent Selectivity for Organic Vapor Sensing. *J. Mater. Chem. C* **2021**, *9*, 5379–5386. https://doi.org/10.1039/D1TC00810B.

(35) Cui, C.; Liu, Y.; Xu, H.; Li, S.; Zhang, W.; Cui, P.; Huo, F. Self-Assembled Metal-Organic Frameworks Crystals for Chemical Vapor Sensing. *Small* **2014**, *10*, 3672–3676. https://doi.org/10.1002/smll.201302983.

(36) Hinterholzinger, F. M.; Ranft, A.; Feckl, J. M.; Rühle, B.; Bein, T.; Lotsch, B. V. One-Dimensional Metal–Organic Framework Photonic Crystals Used as Platforms for Vapor Sorption. *J. Mater. Chem.* **2012**, *22*, 10356. https://doi.org/10.1039/c2jm15685g.

(37) Lu, G.; Farha, O. K.; Kreno, L. E.; Schoenecker, P. M.; Walton, K. S.; Van Duyne, R. P.; Hupp, J. T. Fabrication of Metal-Organic Framework-Containing Silica-Colloidal Crystals for Vapor Sensing. *Adv. Mater.* **2011**, *23*, 4449–4452. https://doi.org/10.1002/adma.201102116.

(38) Ranft, A.; Niekiel, F.; Pavlichenko, I.; Stock, N.; Lotsch, B. V. Tandem MOF-Based Photonic Crystals for Enhanced Analyte-Specific Optical Detection. *Chem. Mater.* **2015**, *27*, 1961–1970. https://doi.org/10.1021/cm503640c.